

See discussions, stats, and author profiles for this publication at: <https://www.researchgate.net/publication/264127643>

Beyond Wenzel and Cassie–Baxter: Second-Order Effects on the Wetting of Rough Surfaces

ARTICLE *in* LANGMUIR · JULY 2014

Impact Factor: 4.46 · DOI: 10.1021/la502143v · Source: PubMed

CITATIONS

3

READS

134

4 AUTHORS, INCLUDING:



[Vahid Hejazi](#)

Rice University

13 PUBLICATIONS 175 CITATIONS

[SEE PROFILE](#)



[Afsaneh Dorri Moghadam](#)

University of Wisconsin - Milwaukee

10 PUBLICATIONS 36 CITATIONS

[SEE PROFILE](#)



[Michael Nosonovsky](#)

University of Wisconsin - Milwaukee

98 PUBLICATIONS 2,964 CITATIONS

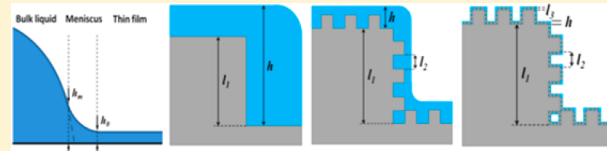
[SEE PROFILE](#)

Beyond Wenzel and Cassie–Baxter: Second-Order Effects on the Wetting of Rough Surfaces

Vahid Hejazi, Afsaneh Dorri Moghadam, Pradeep Rohatgi, and Michael Nosonovsky*

College of Engineering & Applied Science, University of Wisconsin—Milwaukee, Milwaukee, Wisconsin 53211, United States

ABSTRACT: The Wenzel and Cassie–Baxter models are almost exclusively used to explain the contact angle dependence of the structure of rough and patterned solid surfaces. However, these two classical models do not always accurately predict the wetting properties of surfaces since they fail to capture the effect of many interactions occurring during wetting, including, for example, the effect of the disjoining pressure and of crystal microstructure, grains, and defects. We call such effects the second-order effects and present here a model showing how the disjoining pressure isotherm can affect wettability due to the formation of thin liquid films. We measure water contact angles on pairs of metallic surfaces with nominally the same Wenzel roughness obtained by abrasion and by chemical etching. These two methods of surface roughening result in different rough surface structure, thus leading to different values of the contact angle, which cannot be captured by the Wenzel- and Cassie-type models. The chemical and physical changes that occur on the stainless steel and aluminum alloy surfaces as a result of intergranular corrosion, along with selective intermetallic dissolution, lead to a surface roughness generated on the nano- and microscales.



1. INTRODUCTION

The Wenzel and Cassie–Baxter models are generally used in order to describe the wetting properties of rough solid surfaces and, in particular, superhydrophobic surfaces. According to the Wenzel model, liquid fills all roughness cavities, and the wetting regime is homogeneous, whereas according to the Cassie–Baxter model, air pockets are trapped in cavities, which leads to a heterogeneous wetting regime.^{1–8} The Wenzel model states that roughening an intrinsically hydrophobic surface (i.e., contact angle $>90^\circ$) may result in superhydrophobicity with the apparent water contact angle (CA) exceeding 150° . The Cassie–Baxter model states that a combination of trapped air pockets on the surface and surface roughness may lead to superhydrophobicity.^{9,10} Besides a high CA, superhydrophobic surfaces usually have a low sliding angle or CA hysteresis.^{11,12} Although these two models are widely used, the wetting of rough surfaces is much more complex, and involve interactions on various scale levels. Therefore, the two classical models do not always give an accurate prediction of the wetting properties of surfaces.

There are various effects such as contamination, chemical heterogeneity, hierarchical roughness, grains, thin films, the disjoining pressure,^{13–15} and so on which we call the second-order effects. Typically, these effects involve interactions with a length size on the mesoscale. The mesoscale usually refers to distances on the scale of 10 nm to micrometers. However, in relative terms, it is defined at the scale between the nanoscale and the macroscale. The effect of hierarchical and fractal surface roughness (i.e., nanoroughness imposed on microroughness) has been studied by several authors including Cho et al.,¹³ Onda et al.,¹⁶ and Öner and McCarthy.¹⁷

In order to determine the wetting regime in the three-phase system of solid, liquid, and vapor, one has to consider the role of disjoining pressure and the formation of a liquid thin films

(mesoscale layer of the liquid) on the surface of the substrate. Derjaguin first proposed¹⁸ that a liquid thin film, concave liquid meniscus, and a bulk liquid may coexist in an equilibrium conditions (Figure 1a).

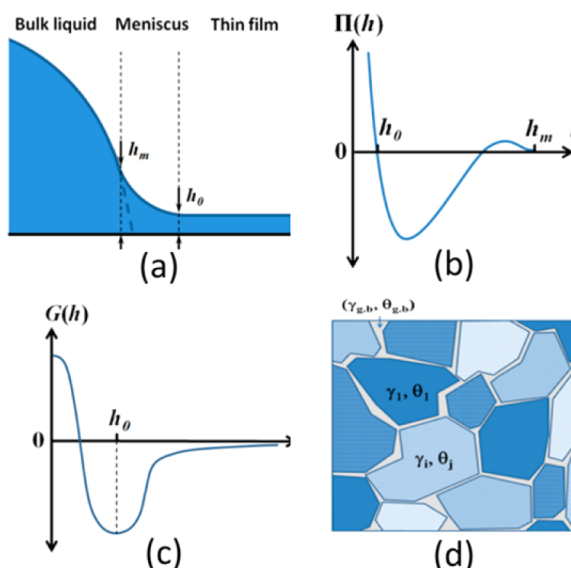


Figure 1. (a) Thin film in equilibrium with the bulk liquid of the droplet. (b) Disjoining pressure isotherm as a function of the film thickness, h . (c) Energy profile of the liquid film. (d) Grain structure with different values of the surface energy and contact angle associated with different grains.

Received: June 6, 2014

Revised: July 20, 2014

Derjaguin defined the disjoining pressure of a liquid thin film as

$$\Pi(h) = -\frac{dG}{dh} \quad (1)$$

where $G(h)$ is the Gibbs free energy per unit area of the film and h is the thickness of the film (Figure 1b). When the film is thick, $h > 100$ nm, the energy of the system corresponds to the summation of solid–liquid (γ_{SL}) and liquid–vapor (γ_{LV}) interfacial energies. However, when $h \rightarrow 0$, the energy of the system corresponds only to the energy of the bare solid (γ_S). Considering these two cases, the energy per unit area can be obtained by¹⁹

$$\frac{\text{energy}}{m^2} = \gamma_{SL} + \gamma_{LV} + G(h) \quad (2)$$

where $G(\infty) = 0$ and $G(0) = \gamma_S - \gamma_{SL} - \gamma_{LV}$.

The main parameter which characterizes the wetting of a solid surface by liquid is the contact angle (CA). Derjaguin derived the relationship between the CA of a liquid droplet placed on a smooth solid surface, θ_0 , and the disjoining pressure as

$$\gamma_{LV} \cos \theta_0 = \gamma_{LV} + \Pi(h_0)h_0 + \int_{h_0}^{\infty} \Pi(h) dh \quad (3)$$

where h_0 is the thickness of the liquid film in equilibrium with the liquid meniscus (Figure 1c) and $\Pi(h_0)$ is the disjoining pressure in the wetting film. Since the value of the disjoining pressure may be positive or negative, the last two terms on the right-hand side of eq 3 play key roles in determining a wetting regime. The negative sign of these two terms corresponds to partial wetting whereas a positive sign corresponds to a complete wetting regime.²⁰ When there is no liquid film ($h = 0$), the energy of the system is equal to the surface energy of the bare solid (γ_S). According to eq 1, the value of disjoining pressure terms in eq 3 should be equal to $G(0)$. Substituting the value of $G(0)$ from eq 2 into eq 3 yields the Young equation.

$$\cos \theta_0 = \frac{\gamma_S - \gamma_{SL}}{\gamma_{LV}} \quad (4)$$

Assuming h_0 to be the film thickness in which the disjoining pressure goes to zero (Figure 1b), we can simplify eq 3 as

$$\cos \theta_0 = 1 + \frac{1}{\gamma_{LV}} \int_{h_0}^{\infty} \Pi(h) dh \quad (5)$$

From eq 5, it is realized that to attain the partial wetting on a smooth surface ($\theta_0 > 0$) the value of h should be between h_0 and h_m ; otherwise, the wetting is complete ($\theta_0 = 0$).

The disjoining pressure is not the only factor that can affect the overall contact angle of the surface and is not taken into account by the standard Wenzel and Cassie–Baxter models. The grain microstructure of polycrystalline metallic materials is another such mesoscale factor. Typically, a metallic surface consists of grains, with a typical size ranging from nanometers to microns, having different orientation. Different crystal planes have different surface energies and therefore different contact angles.²¹ However, it is much more difficult to account for the effect of the grain structure quantitatively than for the effect of the disjoining pressure; therefore, our modeling is concentrated on the latter.

In this study, we present a model dealing with the second-order effects caused by the disjoining pressure and experimental results showing how two surfaces with the same roughness and intrinsic surface energy can have different contact angles, which

we attribute to the second-order effects of surface roughness and heterogeneity on the contact angle.

2. MODELING

In this section we present a model to investigate the wettability of the rough surfaces with multiscale structures considering the effect of disjoining pressure and the liquid thin film at the interface.

In practice, the surfaces are not perfectly smooth but involve microsize protrusions which are covered by nanosize bumps or asperities (Figure 2). These multiscale structures causes

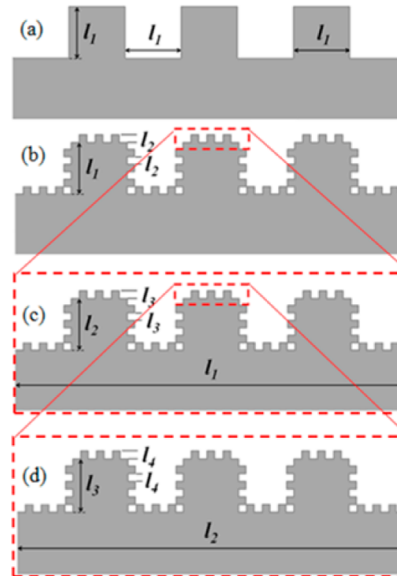


Figure 2. Schematic of a multiscale rough-patterned surface with a hierarchy of details having typical sizes of $l_1 > l_2 > l_3 > l_4$. When a thin film with thickness h_0 is formed, it will cover roughness details with a small size of $l_n > h_0$.

hierarchical roughness. The hierarchical roughness can modify the wettability of the surfaces and result in superhydrophobicity. The lotus leaf is the most popular superhydrophobic plant with hierarchical roughness. There are microscale bumps called papillae on lotus leaves which are covered by nanoscale bumps with sizes less than 100 nm. Here we present a model to study theoretically the wettability of the hierarchical roughened surfaces with the purpose of mimicking a multiscale structure resembling lotus leaves. The effect of disjoining pressure on CA is also considered. In this model, the first order of roughness is considered to be a 2D structure with microscale square pillars of height l_1 separated by a distance l_1 (Figure 2a). It is assumed that the pillars are covered by second-order nanoscale square pillars of height l_2 and spacing l_2 (Figure 2b). Introducing $n = 1, 2, 3, \dots$ as the order of roughness and k as the constant scale ratio, we have

$$\frac{l_1}{l_2} = \frac{l_2}{l_3} = \frac{l_3}{l_4} = \dots = \frac{l_{n-1}}{l_n} = k \quad (6)$$

where l_3, l_4, \dots, l_n are the pillar heights of the third, fourth, and n th orders of roughness (Figure 2c,d). Pillars with an order of roughness greater than 1 (i.e. $n > 1$) possess nanoscale size and affect the surface wettability in a different way from the micro- and macroscale pillars. It is this behavior that we attribute to the second-order effect.

Let us consider a liquid droplet deposited on the above hierarchical roughened surface. The droplet is in equilibrium

with the liquid thin film with a thickness of h . Assuming $h_0 = l_1$, when $h > l_1$, liquid fills all of the cavities between the pillars, and the established wetting regime is Wenzel (Figure 3a). Therefore, the liquid CA is given by

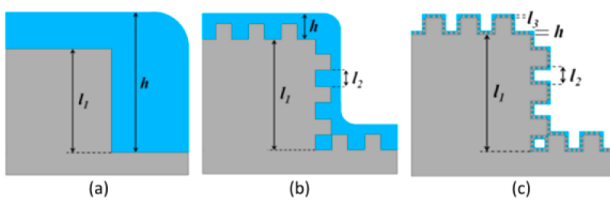


Figure 3. Wetting regimes for multiscales roughness depending on the thickness of the film: (a) all roughness details, (b) some details, and (c) none covered with water.

$$\cos \theta = R_f \cos \theta_0 \quad (7)$$

where the roughness factor $R_f \geq 1$ is the ratio of the real substrate area A_{SL} to the flat projected area A_F and $\cos \theta_0$ is obtained by eq 5. The roughness factor for the square pillars with a constant scale ratio of k and with the structure shown in Figure 2 is given by

$$R_f = 2 \left(\frac{4N + 1}{k} \right)^{n-1} \quad (8)$$

where N is the number of smaller-scale pillars on every side of the larger-scale pillar. Since for the first order of roughness $n = 1$, the value of R_f is equal to 2 and therefore $\cos \theta = 2 \cos \theta_0$ (Figure 3a). Assuming $l_1 = 2 \mu\text{m}$ and $N = 3$, the values of $l_2, l_3, l_4, \dots, l_n$ can be obtained as $l_2 \approx 286 \text{ nm}$, $l_3 \approx 40 \text{ nm}$, $l_4 \approx 6 \text{ nm}$, and so on. For the first order of roughness, it is assumed that $h_m = 14 \mu\text{m}$. Therefore, according to eq 5 and Figure 1b, the equation of disjoining pressure can be approximated as

$$\Pi(h) = (16.8 - 11h + 1.4h^2 - 0.05h^3) \quad (9)$$

where $2 \mu\text{m} < h < 14 \mu\text{m}$.

For the pillars with second order roughness ($n = 2$) (i.e., the smaller pillars), assuming $h_0 = l_2$, when $l_2 < h < l_1$, liquid penetrates between the pillars and fills the smaller-scale cavities with a height of l_2 . The established wetting regime for the pillars on this scale is Wenzel. However, the wetting regime for the pillars with the first order of roughness (larger pillars) is Cassie–Baxter due to the air pockets trapped in the larger-scale cavities with a height of l_1 (Figure 3b). Therefore, the CA is given by

$$\cos \theta = f_{SL} R_f \cos \theta_0 - (1 - f_{SL}) \quad (10)$$

where f_{SL} is the fraction of the solid surface upon which the liquid sits. The value of f_{SL} for the pillars on scales smaller than the first scale ($n > 1$) can be approximated as

$$f_{SL} = \frac{1}{2} \left(\frac{N}{k} \right)^{n-2} \left(1 + \frac{2h}{l_{n-1}} \right) \quad (11)$$

Substituting eqs 8 and 11 into eq 10 gives the liquid contact angle as

$$\begin{aligned} \cos \theta = & \left(\frac{N}{k} \right)^{n-2} \left(1 + \frac{2h}{l_{n-1}} \right) \left(\frac{4N + 1}{k} \right)^{n-1} \cos \theta_0 \\ & - \left(1 - \frac{1}{2} \left(\frac{N}{k} \right)^{n-2} \left(1 + \frac{2h}{l_{n-1}} \right) \right) \end{aligned} \quad (12)$$

For the surface structure shown in Figure 2, $k = 7$ and $N = 3$. Substituting eq 5 into eq 11 and considering the effect of pillars with the second order of roughness ($n = 2$), the liquid CA is given by

$$\cos \theta = \left(1 + \frac{2h}{l_1} \right) \left[\frac{13}{7} \left(1 + \frac{1}{\gamma_{LV}} \int_{h_0}^{\infty} \Pi(h) dh \right) + \frac{1}{2} \right] - 1 \quad (13)$$

According to eq 5 and considering $h_0 = l_2 = 286 \text{ nm}$ and $h_m = 2 \mu\text{m}$, the equation of disjoining pressure can be approximated as

$$\Pi(h) = 0.18 - 0.83h + 0.74h^2 - 0.185h^3 \quad (14)$$

where $286 \text{ nm} < h < 2 \mu\text{m}$.

For the pillars with third order of roughness ($n = 3$), when $l_3 = h_0 < h < l_2$, liquid penetrates between the pillars and fills the smaller-scale cavities with a height of l_3 . The established wetting regime for the pillars on this scale is Wenzel. However, the wetting regime for the pillars with the second order of roughness is Cassie–Baxter due to the air pockets trapped in the larger-scale cavities with a height of l_2 (Figure 3c). Substituting eq 5 into eq 12 and considering the effect of pillars with the third order of roughness ($n = 3$), the liquid CA is given by

$$\cos \theta = \left(\frac{3}{7} \right) \left(1 + \frac{2h}{l_2} \right) \left[\left(\frac{13}{7} \right)^2 \left(1 + \frac{1}{\gamma_{LV}} \int_{h_0}^{\infty} \Pi(h) dh \right) + \frac{1}{2} \right] - 1 \quad (15)$$

According to eq 5 and considering $h_0 = l_3 = 40 \text{ nm}$ and $h_m = 286 \text{ nm}$, the equation of disjoining pressure can be approximated as

$$\Pi(h) = 1.33 - 40.7h + 252.5h^2 - 442.5h^3 \quad (16)$$

where $40 \text{ nm} < h < 286 \text{ nm}$.

To approximate the CA of the liquid droplet considering the effect of pillars with the fourth, fifth, and n th orders of roughness, the value of n corresponding to that desired order should be substituted into eq 12. Figure 4 shows the liquid CA obtained

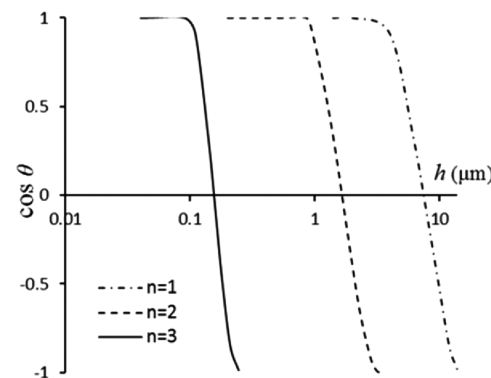


Figure 4. CA versus liquid film thickness, h .

from eqs 7 ($n = 1$), 13 ($n = 2$), and 15 ($n = 3$) versus the liquid film thickness for the pillars with the first, second, and third orders of roughness.

As can be seen in Figure 4, the liquid CA increases differently on pillars with different order of roughness with increasing liquid film thickness, h . The gaps between the CA curves indicate that for the specific values of liquid film thickness only those pillars with orders of roughness in the range of film thickness affect the surface wettability. Comparing the curves for the pillars with first,

second, and third orders of roughness shows that the CA curve for the smallest-scale pillars (third order of roughness) has a steeper slope, indicating that their corresponding CA increases more quickly with increasing film thickness h . For the smaller scale pillars, a higher fraction of the surface is occupied by air pockets, which results in surface energy reduction and therefore CA increase. In addition, for a liquid film thicknesses greater than h_0 , the disjoining pressure is negative. According to eq 1, a negative disjoining pressure implies that the net energy of the interface and therefore the CA are increasing. In the next section, the wettability of the multiscale roughened surfaces is experimentally studied to investigate the distinct behavior of substrates with different scales of roughness.

3. EXPERIMENTAL SECTION

To verify the models presented in the preceding section and observe the influence of second-order effects on wettability, experiments are conducted on aluminum alloy 6061 and 304 stainless steel. These two metals were used because while aluminum is a low-weight, inexpensive, and easy-to-work metal, stainless steel is more corrosion-resistant, easy to clean, and strong.

Some of the methods of creating surface roughness on metal include lithography, etching, deformation, and electroless deposition such as anodization.²² These methods are mostly not easily scalable processes. On the other hand, coating the metal surface with another material to add roughness is a process that often lacks mechanical durability. Therefore, different methods should be sought, such as surface etching with acid solutions. The surfaces of solid materials are often heterogeneous with regard to chemical composition and/or structure. If these heterogeneities occur on suitable length scales and if a selective etching method can be found, it is then possible to create surface roughness on the scale of these microstructural features. Hence by designing a procedure to have selective dissolution on one phase or heterogeneity site, it is possible to create more scalable metal surfaces. In a polycrystalline material, etchant attacks grain boundaries as well as the grains surface to create nanoscale pores, which eventually results in nanoscale structures at the top of the microscale pillars. In this regard, samples were roughened by etching and mechanical abrasion. Mechanical abrasion was used to create microscale roughness whereas chemical etching was applied to create nanoscale roughness. Samples were fabricated, and then the average roughness and liquid CA of them were measured.

3.1. Sample Preparation. Aluminum and stainless steel samples were prepared by sectioning 2-mm-thick metal plates into small square pieces of $2\text{ cm} \times 2\text{ cm}$ size. Samples were then mounted using a hot phenolic mounting machine.

3.2. Mechanical Abrasion. In order to achieve the desired surface roughness, pieces of sand paper with grit sizes of 120, 240, 400, 600, 800, and 1200 were applied. The grit size is a reference to the number of abrasive particles per inch of sandpaper. First, all samples were mechanically abraded using pieces of sand paper from the roughest (grit 120) to the finest (grit 1200) one at a time to obtain glassy, smooth surfaces. Second, to obtain the micro- and nanoscale orders of surface roughness, every aluminum and stainless steel sample was roughened with one of the six grit size pieces sand paper for 30 s by employing an automatic polishing machine. After that, the samples were polished with a soft cloth impregnated with $1\text{ }\mu\text{m}$ alumina. The scanning electron microscope (SEM) images, Hitachi S48000, of the polished samples ground with sand paper to a grit size of 240 are shown in Figure 5.

3.3. Chemical Etching. To simulate the surface roughness induced by corrosive wear, acid etchants were produced. Five milliliters of 96% concentrated sulfuric acid (H_2SO_4), 13 mL of 37% concentrated hydrochloric acid (HCl), and 7 mL of 70% concentrated nitric acid (HNO_3) were mixed to etch the aluminum samples. The solution was then diluted with 20 mL of water. For stainless steel sample etching, the previous solution with an additional 5 mL of 96% concentrated sulfuric acid was prepared. The samples were scrubbed with a chlorine cleanser imbued on a soft cloth. After that, samples were rinsed with water and then dried in air.

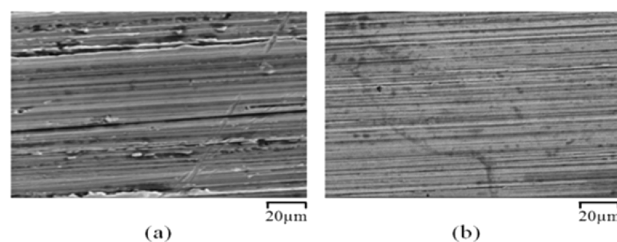


Figure 5. SEM image of abraded samples (grit size 400) (a) aluminum and (b) stainless steel.

The samples were placed in containers containing the specified acid solutions. Six aluminum samples were exposed to the solution for 30, 60, 90, 120, 150, and 180 s, respectively. Stainless steel samples were kept in the solution for 60, 150, 240, 330, 420, and 510 seconds in order to achieve a magnitude of roughness similar to that of the aluminum samples. After that, samples were removed from the solutions, washed with water, and dried with compressed air.

4. RESULTS

The surface roughness of the samples was measured before and after the etching and grinding processes using a surface roughness tester (Phase II+ SRG-4500). For each sample, the surface roughness was calculated by averaging the directional roughness measured on two perpendicular directions on the surface. The roughness parameter measured in the above case is the average roughness value, R_a , defined as the arithmetic average of the absolute values of the roughness profile ordinates.²³ The average roughness values of aluminum and stainless steel samples were 1.1 and $0.14\text{ }\mu\text{m}$ before processing, respectively.

Water CAs were measured before and after etching and grinding. These measurements were made using a model 250 Ramé-Hart standard goniometer/tensiometer. Three water droplets with a $7\text{ }\mu\text{L}$ volumes were applied at different locations on each sample surface, and the final CA was calculated by averaging these three values. CAs of aluminum and stainless steel samples before processing were 69 and 67° , respectively. Figure 6

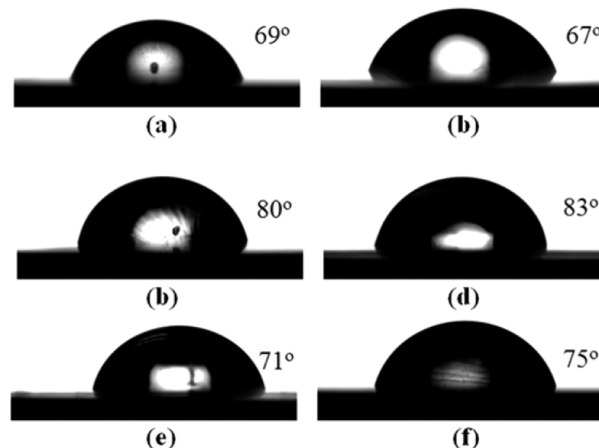


Figure 6. Water droplets on (a) aluminum and (b) stainless steel samples before processing, (c) aluminum and (d) stainless steel after grinding (grit size 400), (e) aluminum after etching (120 s), and (f) stainless steel after etching (5.5 min).

shows the water droplets placed on the aluminum and stainless steel samples before and after etching and grinding.

Figure 7 shows the water CAs of aluminum and stainless steel samples before and after etching and grinding. A theoretical line

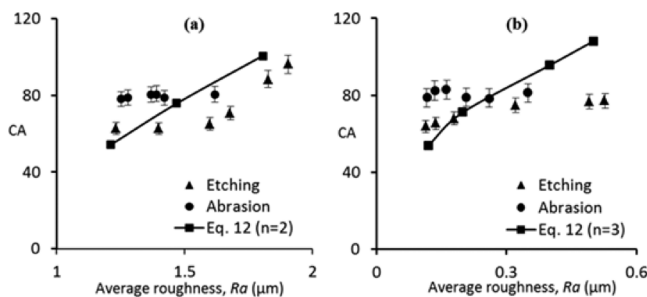


Figure 7. CA versus average roughness, R_a . (a) Aluminum samples and (b) stainless steel samples.

using eq 12 for $R_a = (n - 1)(R_f - 1)$ is also provided. It is observed that the samples with the same magnitude of R_a but with the different methods of roughening have distinct contact angles. This suggests that besides the roughness and chemical heterogeneity of the surface there are various other effects that influence the wetting properties of a surface. While the treatment process may in principle affect the chemical composition of the surface and thus may effect the surface energy and the CA, the effect on surface roughness is much more pronounced. Here, we attribute this distinction to the second scale or hierarchical roughness of the surface.

5. DISCUSSION

Selective etching of the precipitates in the aluminum alloy or selective dissolution of grain and twin boundaries in 304 stainless steel, while leaving the crystalline phase and grains, creates surface roughness on the required length scale. The key advantage of generating roughness directly on a material, as opposed to adding it through the deposition of particles or residues, is the inherent mechanical stability of the structures that are formed via etching.

The microstructure of 304 stainless steel, a chromium–nickel austenitic alloy, is mainly composed of equilibrium and metastable phases which form during solidification. The metastable δ -ferrite phase exists as a skeleton in the austenite matrix after solidification of the 304 stainless steel, which creates microstructural and compositional heterogeneity on the metal surfaces. The etching process would lead to a change in the surface appearance of stainless steel samples from their well-known, shiny silver appearance to dark gray due to the added surface roughness and changes in chemical surface composition. Grain boundaries have higher surface energies compared to grains, and during the etching process, acid solution selectively attacks grain boundaries through intergranular corrosion, thus leading to the formation of micrometer- and submicrometer-scale roughness, creating a multiscale roughness²⁴ that greatly differs from the roughness created in the mechanical abrading step. Intergranular corrosion is caused by the segregation of impurities at the grain boundaries or by enrichment or depletion of one of the alloying elements in the grain boundary. In a corrosive atmosphere, the grain interfaces of these alloys become very reactive and intergranular corrosion results. This is characterized by a localized attack adjacent to grain boundaries with relatively little corrosion of the grains themselves. Once the area around the grains has corroded, the grain will literally fall out. The 304 stainless steel samples microstructure-etched for 60 s in acid solution are shown in Figure 8.

Aluminum alloy 6061 is a precipitation-hardening aluminum alloy containing magnesium and silicon as its major alloying

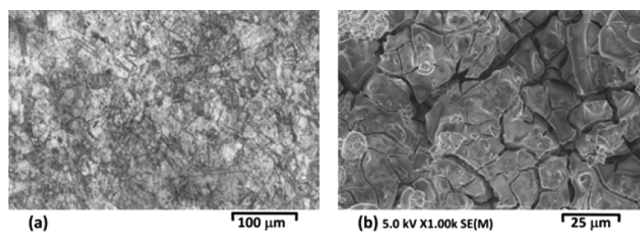


Figure 8. 304 stainless steel samples etched for 60 s: (a) optical image and (b) SEM image.

elements. Several authors have demonstrated that the localized corrosion susceptibility of aluminum alloys is associated with the presence of second-phase particles in the alloy.²⁵ The electrochemical behavior of second-phase particles depends mainly upon the potential difference between the particle and the matrix.²⁶ Two different second-phase particles in aluminum alloy 6061 including active particles rich in magnesium, silicon, and aluminum and particles with iron, silicon, and chromium which show cathodic behavior relative to the aluminum matrix exist.²⁷ The Mg_2Si phase is stable in solutions of pH from 8 to 14 and will undergo selective magnesium dissolution during acid etching.²⁶ This is the reason, a rough surface will form through chemical etching in the order of second phase size, in aluminum alloy 6061. The 6061 aluminum alloy samples microstructure-etched for 60 s in acid solution are shown in Figure 9.

As explained before, the roughness value illustrated in Figure 7 is the average roughness measured by the surface roughness tester with microscale range accuracy. However, as seen from Figure 10, there are numerous nanoscale asperities on top of the microscale asperities which may affect the wetting properties. This nanoscale roughness plays the same role as the nanobumps do at the top of the microbumps on a lotus leaf. The nanobumps are desirable because they prevent water from filling the cavities between the asperities by pinning the nanodroplets.²⁸ Furthermore, the nanoscale surface roughness underneath the water droplet increases the liquid–air fractional area, resulting in reductions in interfacial energy, adhesive force, and contact angle hysteresis. A combination of microscale and nanoscale roughness can help in preventing the air cavities between the asperities from filling with water, even in the case of a hydrophilic material. In particular, the mechanism of the wetting transition from the Cassie–Baxter to Wenzel regime is scale-dependent. To effectively prevent this scale-dependent transition and achieve stable superhydrophobicity, it is expected that a hierarchical roughness is optimum.

To compare the experimental results with the model and determine the wetting property of the surface, the value of the roughness factor, R_f , should be calculated. The roughness factor in eq 6 is defined as the ratio of the real surface area to the flat projected area. Figure 10a illustrates the roughness profile measured in one direction. On the basis of this figure, the roughness factor can be approximated by calculating the length of the profile, squaring the length value, and dividing the result by the flat projected area. As seen in Figure 10, the atomic force microscopy (AFM) is adjusted to draw the roughness profile for $30 \mu\text{m} \times 30$ and $20 \mu\text{m} \times 20 \mu\text{m}$ areas. Therefore, the flat projected areas are $900 \mu\text{m}^2$ and $400 \mu\text{m}^2$. It is noted that the R_f value calculated through the above-mentioned method is the real R_f . However, we need to find the R_f corresponding to only those asperities that significantly affect the wetting regimes.

Depending on the size and pattern of asperities, the liquid phase varies as different shapes such as droplets, channels, and

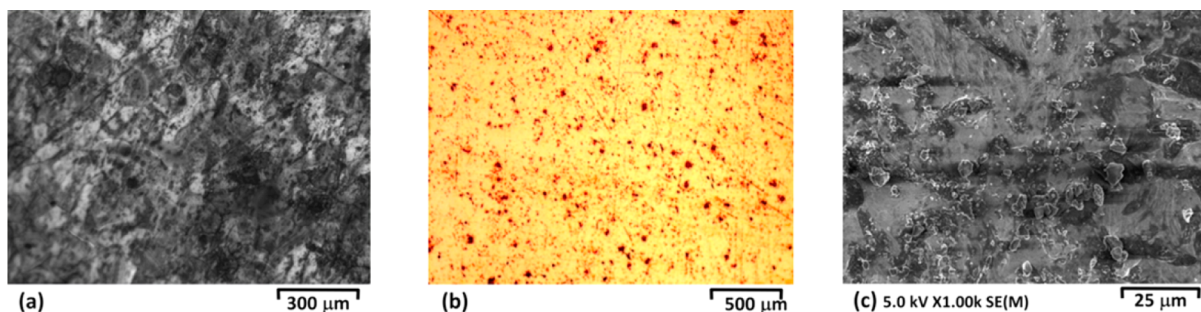


Figure 9. 6061 Al alloy samples etched for 60 s: (a) optical image, (b) polarized light image, and (c) SEM image.

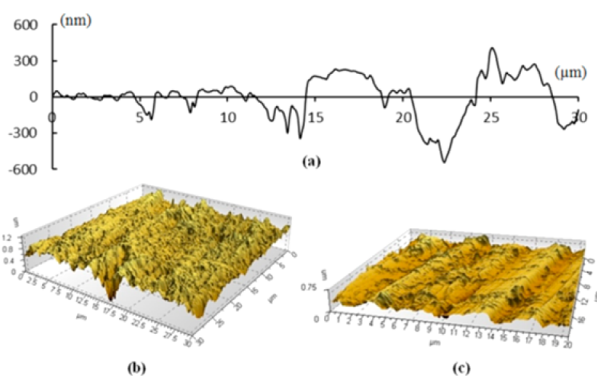


Figure 10. (a) 1D roughness profile, (b) 3D roughness profile of etched aluminum, and (c) 3D roughness profile of abraded aluminum.

thin films to minimize its energy. A thin liquid film with a thickness ranging from a nanometer to less than a micrometer can form at the surface. The surface energy of the film can be determined by calculating the change in total energy when the surface area of the film varies by a small amount. Thus, the surface energy of the film is given by¹⁹

$$\gamma_h = \gamma_{SL} + \gamma_{LV} + G(h) + \Pi(h)h \quad (17)$$

The liquid film is stable when the curvature of the disjoining pressure isotherm sketched in Figure 1c is positive ($\ddot{G}(h) > 0$), indicating the coexistence of a droplet with a liquid film of thickness h_0 . Should there be an inadequate liquid supply to continuously retain the liquid film ($h < h_0$), the droplet can spread over the entire surface. The surface micro/nanostructure can change the impact of the liquid film on the wetting properties in an important way. For the nanoscale structures, the macroscopic laws are not valid anymore and the effects of intermolecular forces, capillary action, and disjoining pressure should be applied.^{29,30} Micro/nanoscale asperities of the rough surface minimize the free energy of the interface by reducing the solid–liquid contact area which leads to an increased contact angle.

However, considering the role of disjoining pressure and the formation of a liquid thin film on the substrate, indeed a large number of nanoscale asperities covered by the liquid film do not directly affect the energy of the interface because they are already in the Wenzel regime. However, those asperities with a height greater than the film thickness still have the potential to trap air pockets, resulting in the Cassie–Baxter regime. Therefore, only a small portion of the nanoscale asperities in R_f , which are called the effective asperities, affect the wetting regimes. The roughness factor corresponding to the effective asperities is called the effective roughness, R_{eff} . In order to verify the distinct values of contact angles for etched and abraded samples shown in Figure 7, one needs to measure the exact value of R_{eff} for the samples. Since

the surface is random to some extent, the exact surface topography is not known. Therefore, calculating the exact value of R_{eff} may be difficult. This makes the investigation of the wetting property of a rough surface a much more complex process, which cannot be simply predicted by the two classical models of Wenzel and Cassie–Baxter.

6. CONCLUSIONS

The wettability of the rough, solid substrates can be much more complex than what is predicted by the two classical models of Wenzel and Cassie–Baxter. Various effects occurring at the mesoscale influence the wettability of the rough solid surfaces. We developed a model to investigate the wettability of the rough surfaces with multiscale structures considering the effect of disjoining pressure and the liquid thin film at the interface. We also experimentally studied the influence of second-order effects on the wettability of such surfaces. We introduced the effective roughness factor, R_{eff} , as the fraction of R_f corresponding to the asperities with a height greater than the film thickness which have the potential to trap air pockets, resulting in the Cassie–Baxter regime.

■ AUTHOR INFORMATION

Corresponding Author

*E-mail: nosonovs@uwm.edu. Tel: +1-414-229-2816. Fax: +1-414-229-6958.

Notes

The authors declare no competing financial interest.

■ ACKNOWLEDGMENTS

We acknowledge gratefully the support of the UWM RGI and NSF I/UCRC for a water equipment and policy grant and grant NSF-MIL-107834.

■ REFERENCES

- (1) Choi, C.-H.; Kim, C.-J. Droplet evaporation of pure water and protein solution on nanostructured superhydrophobic surfaces of varying heights. *Langmuir* **2009**, *25*, 7561–7567.
- (2) Li, W.; Amirfazli, A. Hierarchical structures for natural superhydrophobic surfaces. *Soft Matter* **2008**, *4*, 462–466.
- (3) Kietzig, A. M.; Hatzikiriakos, S. G.; Englezos, P. Patterned superhydrophobic metallic surfaces. *Langmuir* **2009**, *25*, 4821–4827.
- (4) Bormashenko, E. Y. *Wetting of Real Surfaces*; De Gruyter: Berlin, 2013.
- (5) Nosonovsky, M.; Bhushan, B. Superhydrophobic surfaces and emerging applications: non-adhesion, energy, green engineering. *Curr. Opin. Colloid Interface Sci.* **2009**, *14*, 270–280.
- (6) Nosonovsky, M. Materials science: Slippery when wetted. *Nature* **2011**, *477*, 412–413.

- (7) Tadmor, R.; Bahadur, P.; Leh, A.; N'guessan, H. E.; Jaini, R.; Dang, L. Measurement of lateral adhesion forces at the interface between a liquid drop and a substrate. *Phys. Rev. Lett.* **2009**, *103*, 266101(1-4).
- (8) Tadmor, R. Approaches in wetting phenomena. *Soft Matter* **2011**, *7*, 1577–1580.
- (9) Nosonovsky, M.; Hejazi, V. Why superhydrophobic surfaces are not always icephobic. *ACS Nano* **2012**, *6*, 8488–8491.
- (10) Hejazi, V.; Sobolev, K.; Nosonovsky, M. From superhydrophobicity to icephobicity: forces and interaction analysis. *Sci. Rep.* **2013**, *3*, 2194.
- (11) Hejazi, V.; Nosonovsky, M. Contact angle hysteresis in multiphase systems. *Colloid Polym. Sci.* **2013**, *291*, 329–338.
- (12) Extrand, C. W.; Kumagai, Y. J. An Experimental Study of Contact Angle Hysteresis. *Colloid Interface Sci.* **1997**, *191*, 378–383.
- (13) Cho, K.L.; Wu, A. H. F.; Liaw, I.I.; Cookson, D.; Lamb, R. N. Wetting Transitions on Hierarchical Surfaces. *Phys. Chem. C* **2012**, *116*, 26810–26815.
- (14) N'guessan, H. E.; Leh, A.; Cox, P.; Bahadur, P.; Tadmor, R.; Patra, P.; Vajtai, R.; Ajayan, P.M.; Wasnik, P. Water tribology on graphene. *Nat. Commun.* **2012**, *3*, 1242.
- (15) Belman, N.; Jin, K.; Golani, Y.; Israelachvili, J. N.; Pesika, N. S. Origin of the contact angle hysteresis of water on chemisorbed and physisorbed self-assembled monolayers. *Langmuir* **2012**, *28*, 14609–14617.
- (16) Onda, T.; Shibuichi, S.; Satoh, N.; Tsujii, K. Super-Water-Repellent Fractal Surfaces. *Langmuir* **1996**, *12*, 2125–2127.
- (17) Öner, D.; McCarthy, T. J. Ultrahydrophobic Surfaces. Effects of Topography Length Scales on Wettability. *Langmuir* **2000**, *16*, 7777–7782.
- (18) Derjaguin, B.V. *Acta Physicochim. URSS* **1940**, *12*, 171.
- (19) Gennes, P. D.; Brohard-Wyart, F.; Quéré, D. *Capillarity and Wetting Phenomena: Drops: Bubbles, Pearls, Waves*; Springer: New York, 2004.
- (20) Boinovich, L.; Emelyanenko, A. Wetting and surface forces. *Adv. Colloid Interface Sci.* **2011**, *165*, 60–69.
- (21) Murr, L. E. *Interfacial Phenomena in Metals and Alloys*; Addison-Wesley: Reading, MA, 1975.
- (22) Roach, P.; Shirtcliffe, N. J.; Newton, M. I. Progress in superhydrophobic surface development. *Soft Matter* **2008**, *4*, 224–240.
- (23) Taha, Z.; Lelana, H. K.; Aoyama, H.; Ariffin, R.; Gonzales, J.; Sakundani, N.; Bhakti, S. *Effect of Insert Geometry on Surface Roughness in the Turning Process of AISI D2*. Proceedings of the 11th Asia Pacific industrial Engineering and Management Systems Conference, Melaka, Malaysia, 2010.
- (24) Li, L.; Breedveld, V.; Hess, D. W. Creation of superhydrophobic stainless steel surfaces by acid treatments and hydrophobic film deposition. *ACS Appl. Mater. Interfaces* **2012**, *4*, 4549–4556.
- (25) Foley, R. T. Localized corrosion of aluminum alloys- a review. *Corrosion* **1986**, *42*, 277–288.
- (26) Linardi, E.; Haddad, R.; Lanzani, L. Stability Analysis of the Mg₂Si Phase in AA 6061 Aluminum Alloy. *Procedia Mater. Sci.* **2012**, *1*, 550–557.
- (27) Alodan, M. A.; Smyrl, W. H. Detection of localized corrosion of aluminum alloys using fluorescence microscopy. *J. Electrochem. Soc.* **1998**, *145*, 1571–1577.
- (28) Bhushan, B.; Jung, Y. C.; Koch, K. Micro-, nano- and hierarchical structures for superhydrophobicity, self-cleaning and low adhesion. *Philos. Trans. R. Soc., A* **2009**, *367*, 1631–1672.
- (29) Dietrich, S.; Popescu, M. N.; Rauscher, M. Wetting on structured substrates. *J. Phys.: Condens. Matter* **2005**, *17*, S577–S593.
- (30) Bonn, D.; Eggers, J.; Indekeu, J.; Meunier, J.; Rolley, E. Wetting and Spreading. *Rev. Mod. Phys.* **2009**, *81*, 739–805.